The influence of realistic 3D viscous mean flow on shielding of engine-fan noise by a 3-element high-lift wing

J. Dierke* and R. Ewert*
Institute of Aerodynamics and Flow Technology, Technical Acoustics
German Aerospace Center (DLR),
Lilienthalplatz 7, 381208 Braunschweig, Germany
and J. Chappuis† S. Lidoine† and J. Ricouard †
AIRBUS Operations SAS,
316 route de Bayonne, 31060, TOULOUSE, Cedex 09, France

The prediction of aeroacoustic shielding often rests on tools using constant mean flow thus neglecting mean flow inhomogeneities such as shear layers. This study analyses the influence of this simplification on shielding. As an example we considered engine-fan noise shielding at a 3-element high-lift wing. A Computational Aeroacoustic (CAA) approach was chosen. The simulations were carried out with the DLR CAA code PIANO. PIANO solves the Linearized Euler Equations (LEE) over steady viscous mean flow. To determine the mean flow influence three sets were computed. One rests on a realistic viscous Reynolds Averaged Navier-Stokes (RANS) solution, the second makes use of a simple constant mean flow and the third uses constant mean flow in conjunction with a flat plate with the same chord length to replace the wing. An axisymmetric solution of the finite element simulation code ACTRAN predicted the fan sound propagation from the engine intake through the non-uniform flow to a cylindrical interface. Subsequently, the data was coupled to the CAA computational domain via a Thompson boundary condition. It is shown that this condition meets the coupling requirements well. This study shows that the viscous mean flow has a significant influence on the predicted shielding potential of a high-lift wing. That is, the shielding benefit of a simplified prediction based on uniform flow propagation and a simplified geometrical significantly overestimate the potential shielding benefits considerably.

Nomenclature

J	Jacobean matrix
ρ'	Perturbation density
p'	Perturbation pressure
$\vec{v}'$	Perturbation velocity vector
dB	Decibels
SPL	Sound pressure level [dB]
f	Shielding/Attenuation factor [-]
c	chord length
κ	adiabatic exponent
m	azimuthal fan mode
n	radial fan mode

Subscript

*Research Scientist, Technical Acoustics, email:juergen.dierke@dlr.de, and AIAA Member
†EDEA - Acoustics and Environment Dpt.,Aircraft Acoustics Integration

0 indicates mean flow values

I. Introduction

Developing quieter aircrafts is essential to enable the continuous growth of air traffic in the future. Engine noise represents still one of the main noise sources. To achieve during take-off a reduction of engine noise emission towards the ground two alternative measures are possible. Besides reducing engine sound emissions directly, as an alternative or additional approach one may utilize the blocking or shielding effect of aircraft components such as wing, fuselage, or empennage on radiated engine noise. Work on predicting acoustic shielding has been conducted by various authors. Jones[5] derived analytic solutions for simple flows and geometries. More complex flow fields were studied by Howe.[3] Scattering in quiescent medium can be covered by the Boundary Element Method (BEM).[11] Among others Clancy and Rice[1] tried to extend the method for low frequencies to non-uniform mean flow. To exactly predict sound propagation of small disturbances through non-uniform flow it is necessary to use finite differences or finite element codes. For example the diffraction of aft fan noise at over-wing nacelle configurations was reported by Redonnet et al.[10]

The intention of this study is to estimate the influence of non-uniform mean flow on shielding. This is accomplished by comparing shielding predictions for sound propagation through a constant mean flow against solutions with viscous RANS mean flow. As a test problem the shielding of rear-mounted engine fan noise by a 3-element high-lift wing is considered. A generic geometry, based on a non-tapered unswept high-lift wing is used. It consists of a slat, wing and flap in take-off position. In the framework of the EU Project NACRE the engine fan noise source is provided by Airbus Operations SAS on a finite length cylinder surface with rounded caps, which encloses the engine. An axial symmetric finite element simulation code predicted the fan sound propagation from the engine intake through the non-uniform flow to the cylinder surface. This simulations delivered acoustic pressure on the cylinder surface and pressure gradients normal to the surface for a set of different intake duct modes. In Fig. 1 the configuration of the engine enclosing cylinder and the high-lift wing is depicted. In a subsequent step, this data is used by DLR to simulate in 3D noise shielding with its computational aeroacoustic (CAA) code PIANO.

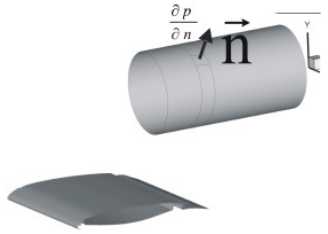

Figure 1. *Sketch of the cylinder surface where the pressure and its normal derivative of the engine fan noise is given*

II. Computational Approach

The shielding computations are conducted with the finite differences code PIANO solving the Linearized Euler Equations (LEE). Underlying the acoustic computation is a constant mean flow or a viscous mean flow. The viscous mean flow is a RANS solution. The propagation through the engine to the engine surrounding cylinder is computed with the axial symmetric solver ACTRAN. The noise data on the cylinder surface is the sound pressure and its derivative normal to the surface for different azimuthal and radial modes. This data is injected into the CAA domain via a Thompson boundary condition. Using a characteristic boundary condition as interface has already been performed successfully by Kim and Lee.[6–8] To summarize, there are two computational domains: one containing the engine limited by the cylinder surface and one containing the high-lift wing connected due to a Thompson boundary condition. ACTRAN works in the first domain and PIANO in the second one. The domain and their connections are displayed in Fig. 2.

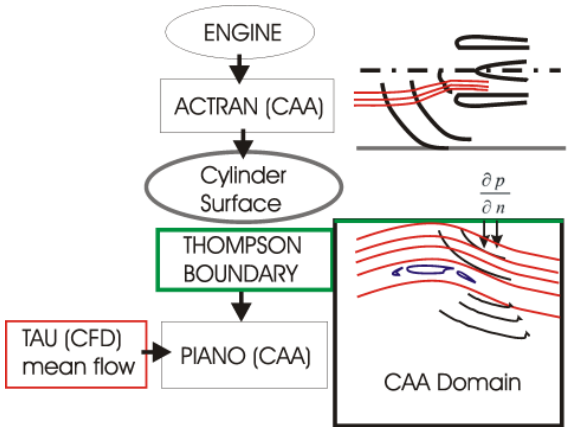

Figure 2. *Sketch of programs and interfaces for shielding computations.*

A. ACTRAN

Isolated fan forward noise results have been computed by Airbus with ACTRAN FEM solver assuming a potential mean flow for different modes at 3 regimes. The mean flow has been computed by Euler CFD computations. The Fig. 3 shows the Mach number values in the inlet in the case of an external flow of M=0.18 and the corrected regime equal to 32000rpm. On this figure is also plotted the position of the interface where pressure and velocity have been calculated by ACTRAN solver and transferred to DLR for the PIANO computations.

The validation of the ACTRAN code for inlet radiation with non uniform has been published in ref.[9] This study addressed the validation of both hardwall and lined intakes predictions by comparisons with test rig data.

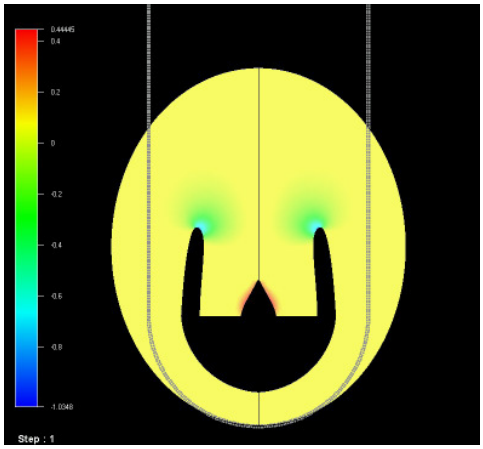

Figure 3. *Mach number values in the inlet in the case of an external flow of M=0.18 and the corrected regime equal to 32000rpm*

B. RANS Simulations

The RANS calculations have been performed with the DLR Code TAU. TAU is an unstructured solver. The numerical grid comprises 90000 points. The boundary layer is resolved by 55 nodes. The first interior point is located at $y^+ \leq 1$ from the airfoil surface, yielding a sufficient resolution of the viscous sublayer. Farfield boundaries are located 20 chord lengths (c) away from the airfoil. As shown in Fig. 4 the grid is normalized with c. The RANS computations have been conducted using a Menter SST model. The Mach number was 0.3 and the Reynolds number $13. \cdot 10^6$ with an angle of attack of 2°.

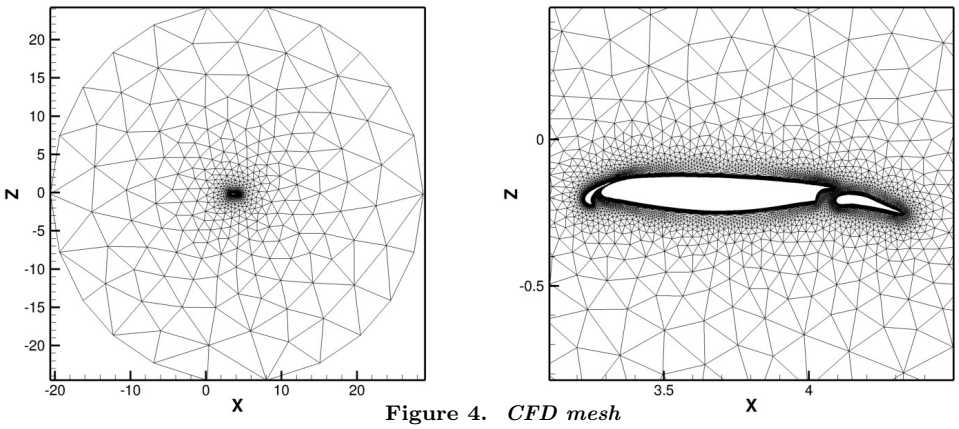

Figure 4. *CFD mesh*

C. CAA Simulations

For the shielding simulation the aeroacoustic code PIANO[2] of DLR is used to resolve the acoustic propagation over a viscous time-averaged turbulent flow solution. The Linearized Euler Equations (LEE) are applied as governing equations (Eq. 1). They are equivalent to the linearized Navier-Stokes equations neglecting viscous perturbations. PIANO applies curvilinear structured grids. Spatial gradients are approximated using the dispersion relation preserving (DRP) scheme proposed by Tam and Webb.[12] The temporal discretization is achieved with the 4th-order low-dispersion Runge-Kutta (LDDRK) algorithm proposed by Hu.[4] As a mean-flow the RANS solution for a high-lift geometry with take-off settings is used. The differential equation system has the following

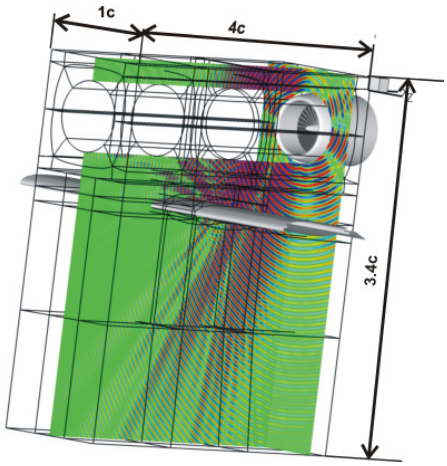

Figure 5. *Computational domain consists out of 178 blocks and 25 million points; black lines are edges of the blocks; instantaneous pressure perturbation is depicted on slices.*

form:

$$\frac{\partial \rho'}{\partial t} + \vec{v} \cdot J\nabla_\xi \rho_0 + \vec{v}_0 \cdot J\nabla_\xi \rho' + (J\nabla_\xi) \cdot \vec{v}_0 \rho' + (J\nabla_\xi) \cdot \vec{v}' \rho_0 = 0$$

$$\frac{\partial \vec{v}'}{\partial t} + \vec{v}' \cdot J\nabla_\xi \vec{v}_0 + \vec{v}_0 \cdot J\nabla_\xi \vec{v}' + \frac{J\nabla_\xi p'}{rho_0} - \frac{J\nabla_\xi p_o \rho'}{\rho_0^2} = 0 \quad (1)$$

$$\frac{\partial p'}{\partial t} + \vec{v} \cdot J\nabla_\xi p_0 + \vec{v}_0 \cdot J\nabla_\xi p' + \kappa \left[(J\nabla_\xi) \cdot \vec{v}_0 p' + (J\nabla_\xi) \cdot \vec{v}' p_0 \right] = 0$$

J is the Jacobean and the primed quantities denote the perturbation variables, whereas the subscript "0" indicates mean flow variables.

MESH

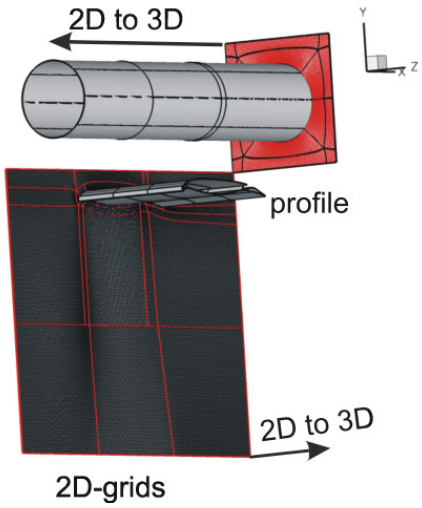

Figure 6. ***CAA grid built by assembling two extruded 2D meshes***

A CAA mesh was built, resolving the wing and comprising a circular hole in stream wise direction above the wing, whose wall surface defines the data sampling surface. The mesh consists of two main parts. Each of these 3D topologies were generated by extruding a 2D-mesh.

The CAA domain is built out of 178 blocks with 25 million points and has the dimensions of $3c$ in x-direction, $1c$ in span wise direction and $3.4c$ upwards. The engine inlet center is located $1.7c$ behind the clean wing leading edge and $0.7c$ above the wing. The non-dimensionalized wave number of the engine fan is 99.

D. Thompson boundary condition

Since only acoustic surface data was available on the cylinder surface, a one-layer boundary condition (BC) has been employed to couple the acoustic waves into the CAA domain. For this an extended Thompson boundary condition[14,15] was implemented into the CAA-Code. The Thompson boundary condition is a radiation and outflow boundary condition. It is based on the transformation of the hyperbolic LEEs into their characteristic form. The Thompson BC divides the LEE into incoming and outgoing waves. The LEE posses five characteristic waves in 3D, refer to Fig. 7. The eigenvalues of the system correspond to the respective wave's speeds; the wave velocities are written in braces. For each boundary point it is possible to decide whether the wave is incoming or outgoing. By setting the incoming parts to zero the boundary behaves like a radiation or outflow boundary condition.

The LEE can be written as

$$\frac{\partial \vec{U}}{\partial t} = \overline{A}_\xi \frac{\partial \vec{U}}{\partial \xi} + \overline{A}_\eta \frac{\partial \vec{U}}{\partial \eta} + \overline{A}_\zeta \frac{\partial \vec{U}}{\partial \zeta} + \overline{C} \quad (2)$$

with the perturbation variables vector $\vec{U} = (\rho', u', v', w', p')^T$. $\bar{C}$ are terms with mean flow derivatives only. For each face of a block with Thompson boundary the adequate Matrix $\overline{A_\xi}$ will be decomposed into its left eigenvectors $\overline{S}$ (Matrix with left eigenvectors (row)) and right eigenvectors $\overline{S}^{-1}$ (Matrix with right columnwise eigenvectors).

$$\bar{S}\bar{A}\bar{S^{-1}} = \bar{\Lambda} \quad (3)$$

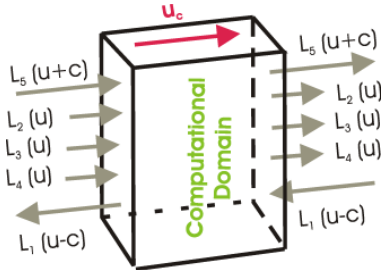

Figure 7. ***Scheme of the computational domain with its eigenvectors.***

$\overline{\Lambda} = diag(\lambda_1, \lambda_2, \lambda_3, \lambda_4, \lambda_5)$ is a diagonal matrix containing the eigenvalues. The matrix $\bar{A}_\xi$ for the LEE looks like

$$\bar{A}_\xi = \begin{pmatrix} a_{ii} & \xi_x \rho_0 & \xi_y \rho_0 & \xi_z \rho_0 & 0 \\ 0 & a_{ii} & 0 & 0 & \xi_x \frac{1}{\rho_0} \\ 0 & 0 & a_{ii} & 0 & \xi_y \frac{1}{\rho_0} \\ 0 & 0 & 0 & a_{ii} & \xi_z \frac{1}{\rho_0} \\ 0 & \xi_x \kappa p_0 & \xi_y \kappa p_0 & \xi_z \kappa p_0 & a_{ii} \end{pmatrix} \quad (4)$$

with the contravariant velocities

$$a_{ii} = \xi_x u_0 + \xi_y v_0 + \xi_z w_0$$

for ξ-direction. The boundary condition analysis becomes more convenient introducing a vector $\vec{L}$ with its components L_i by

$$L_i := \lambda_i \vec{l_i}^T \frac{\partial \vec{U}}{\partial \xi} \tag{5}$$

where $\vec{l_i}^T$ is the transposed "i"th left eigenvectors of $\vec{A_\xi}$ i.e. the $\vec{l_i}^T$ are the rows of $\bar{S}$. To solve the characteristic linear Euler equations the product $\vec{d} := \bar{S}\vec{L}$ is required. The purpose of boundary conditions is to supply whatever information is needed at the boundaries of the computational volume in order to complete the definition of the behavior of the system. Each eigenvalue λ_i represents the characteristic velocity at which a particular wave mode propagates. If the velocity λ_i indicates an outgoing wave, L_i is calculated as described above. If it indicates an incoming wave L_i must be chosen so that it satisfies the boundary condition.

It is also possible to set the incoming parts to specific periodic values to inject a solution into the CAA domain. Therefore the pressure normal derivatives have to be available at the boundary points.

Boundary test

The boundary condition and its implementation are tested with a problem akin to the category 3 benchmark problem 1 defined for the first workshop on CAA benchmark problems.[13] The benchmark consists of a domain with non-dimensionalised dimensions 100×100 consisting out of 101×101 points with the domain's limits at $(-50, -50)$ and $(50, 50)$. The constant mean flow is in x-direction with a Mach number of 0.5. As initial condition a pressure pulse, an entropy pulse and a vortex are placed at (x_a, y_a), (x_b, y_b) and (x_b, y_b), respectively. The positions are chosen such that the different waves reach the outflow boundary simultaneously, i.e. $(x_a, y_a) = (-25, 0)$ and $(x_b, y_b) = (+25, 0)$. The spatial contributions are as follows:

$$p' = exp\left[-(ln2)\left(\frac{\pi(\vec{x} - \vec{x_a})^2}{9}\right)\right] \tag{6}$$

$$\rho' = exp\left[-(ln2)\left(\frac{\pi(\vec{x} - \vec{x_a})^2}{9}\right)\right] + 0.1exp\left[-(ln2)\left(\frac{\pi(\vec{x} - \vec{x_b})^2}{25}\right)\right] \tag{7}$$

$$u' = 0.04(y - y_b)exp\left[-(ln2)\left(\frac{\pi(\vec{x} - \vec{x_b})^2}{25}\right)\right] \tag{8}$$

$$v' = 0.04(x - x_b)exp\left[-(ln2)\left(\frac{\pi(\vec{x} - \vec{x_b})^2}{25}\right)\right] \tag{9}$$

The results depicted in Fig. 8 show small reflections, but the perturbations can pass the boundaries well.

Another test setup is used to analyze the injection behavior of the boundary condition. The set up is shown in Fig. 9. It consists of a monopole with a nondimensionalized wavenumber of $k = 10$ located above the computational domain at (0/1.2/0). The computational domain has the dimensions $4 \times 1 \times 1$. The domain's boundaries are sponge layers in x and z-direction. The injecting boundary is the Thompson boundary opposite to the slip wall indicated at the bottom of Fig.9. The underlying mean flow is a constant with a Mach number of 0.75. A snapshot of the pressure field is shown in Fig. 9. The contour colors display the numeric solution of the instantaneous pressure perturbation and the iso contour lines are plotted for the analytic solution. The agreement between the two solutions is quite satisfying.

III. Simulation set up

There are four simulation set-ups, which are sketched in Fig. 10. One set-up consists of the CAA computational domain with constant mean flow, but without any shielding surface. This is the set-up the shielding cases are compared with. There are in total 3 shielding cases. Shielding case "A" consists of a plate replacing the high-lift wing with a constant mean flow. Case "B" makes use of the 3-element high-lift wing and a constant mean flow. The third case, shielding case "C" combines a 3D viscous RANS mean flow

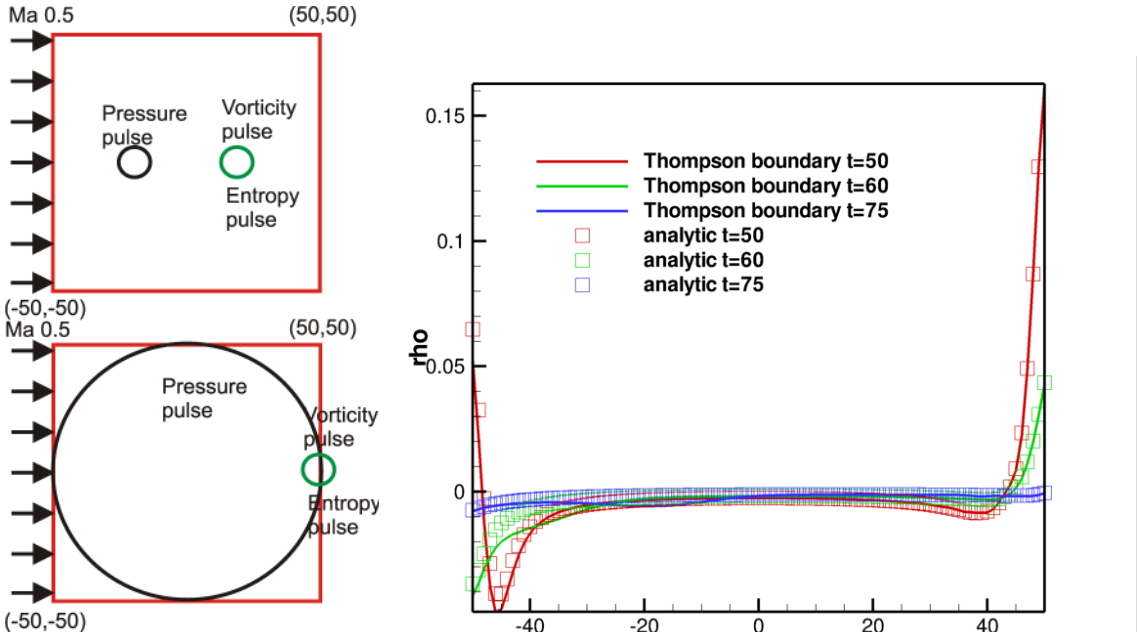

Figure 8. *Sketch of the benchmark case for t=0 (top left) and t=50 (bottom left). The right figure shows the numerical results and the analytical results for a line at* $y = 0$.

m	0	1	2	3	4	5	6	7	8	9	10	11	12	13	14	15	all
n	1-4	1-4	1-4	1-4	1-4	1-4	1-3	1-3	1-2	1-2	1-2	1-2	1	1	1	1	all
no.	4	4	4	4	4	4	3	3	2	2	2	2	1	1	1	1	42

Table 1. *Computations made for different engine modes; m = azimuthal fan mode, n = radial fan mode, no. = no. of modes in one computation*

with the 3-element high-lift wing. The clean wing (without deployed flaps) is located between (0/0) and (1/0). The engine inlet center is located at (1.7/0.7). The mean flow Mach number is 0.3.

Computations for all set-ups were made with 42 different intake-duct fan modes. Table 1 shows the used fan mode combinations. 16 azimuthal fan modes (m) were taken into account and 4 radial modes (n). For each set-up 16 computations have been performed whereby the radial modes were summed up for each azimuthal mode.

IV. Results & Conclusion

The efficiency of shielding is quantified by the shielding factor f. It is defined by $f = \frac{p_{RMS,geo}}{p_{RMS,free}}$ with $p_{RMS,geo}$ as the effective pressure at the observer position with geometry present and $p_{RMS,free}$ as the effective pressure at the observer position with geometry absent. In figure 11 the sound pressure level differences ($\Delta SPL = 10 * log10(f)$) are depicted for a slice at z = 0 (through the engine axis) for the three shielding cases. In the left picture the contour colors show the shielding levels with a flat plate and a constant Mach number of 0.3. The black lines are SPL iso-lines for the engine sound radiation without obstacles, i.e. the fan noise directivity. This is important to avoid misinterpretation of the shielding levels, because it is possible that by diffraction part of the sound energy is radiated into regions which in the free field case are not reached by sound waves. In that case ΔSPL would be positive, but the original SPL at that point is very small. Hence, the overall sum of original SPL and ΔSPL is tolerably small, even if positive ΔSPL values are encountered.

Fig. 12 presents shielding levels for the flat plate and the wing, both for constant mean flow, and for the wing with viscous RANS mean flow over all emission angle Θ on an observer circle with radius 2 c. This example is for the azimuthal mode 0 and the four radial modes 1-4. The shielding levels show nearly the

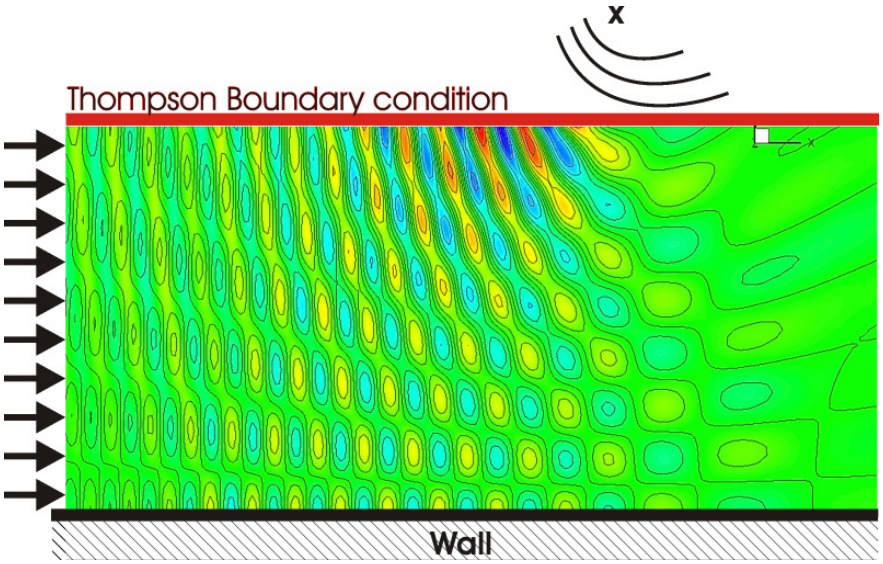

Figure 9. *Instantaneous acoustic pressure perturbations: The CAA solution is shown as contour, the analytic solution is shown as lines.*

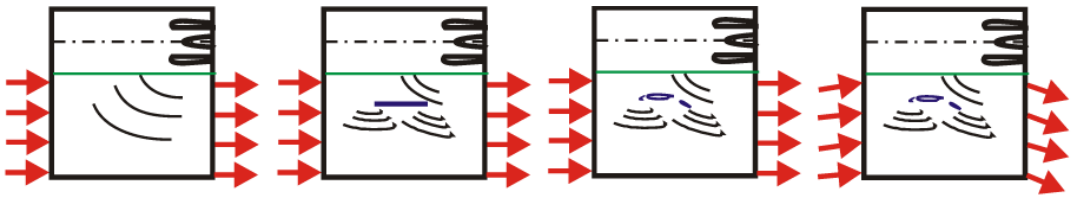

Figure 10. *Sketches for different experimental setups: "'freestream"', shielding case "A", "B", "C"*

same characteristics for the flat plate and the wing with constant mean flow over the observer angles. The SPL reduction in an angle interval between 22° and 50° is around 25 dB. The results for the shielding with RANS mean flow show the same trends, but the shielding benefit exhibits a significant smaller level yielding up to $-10dB$ differences to the simplified computation.

All results for each modal combination listed in figure 1 are shown in figures 13-24. As before the $\Delta SPLs$ for the 3 shielding cases are depicted as contour plots for the x-y planes. The isocontours of the free field sound pressure level are drawn as black lines thus indicating the areas in which the ΔSPL is relevant. In the fourth picture the ΔSPL is plotted against the emission angle for the 3 shielding cases. The yellow highlighted area is, as before, the area which is in the direct line of sight of the shielding geometry.

Analyzing the results with respect to the main free field emission direction it is observed that for higher azimuthal modes the main emission direction moves further backward. For the cases of azimuthal mode orders $m = 1$ to 4 the emission directly irradiates onto the profile. For modes $m = 5$ and 6 only the rear section of the profile is affected. Only a small part emitted by modes $7 - 10$ is approaching the flap. The higher modes nearly miss the profile just touching the trailing edge.

The interesting angle interval for shielding is between 22° and 50°, therefore the following analyses are made only for this area. The sound pressure level reduction due to the flat plate is around 25 dB for the azimuthal modes 0 and 1. The ΔSPL reduction for higher modes up to $m = 8$ is around $10 - 15dB$ in the emission direction. An increase of the sound pressure level of around $20dB$ occurs for the modes $9 - 11$, but not in emission direction. Equal results can be observed for the modes $12 - 15$, not shown here. The ΔSPL for the shielding case "B" are similar to the ones for case "A" set-up. The main differences are some shielding peaks at specific frequencies. The sound pressure level reduction for the shielding case "C" with viscous mean flow considerable differs from case "B". For the azimuthal mode 0 the reduction is only around 10 dB in contrast to 20 to 25 dB for the constant mean flow case. The modes 1-6 show a reduction only in an angle interval for low angles up to 40°. At higher angles they show nearly the same reduction as the

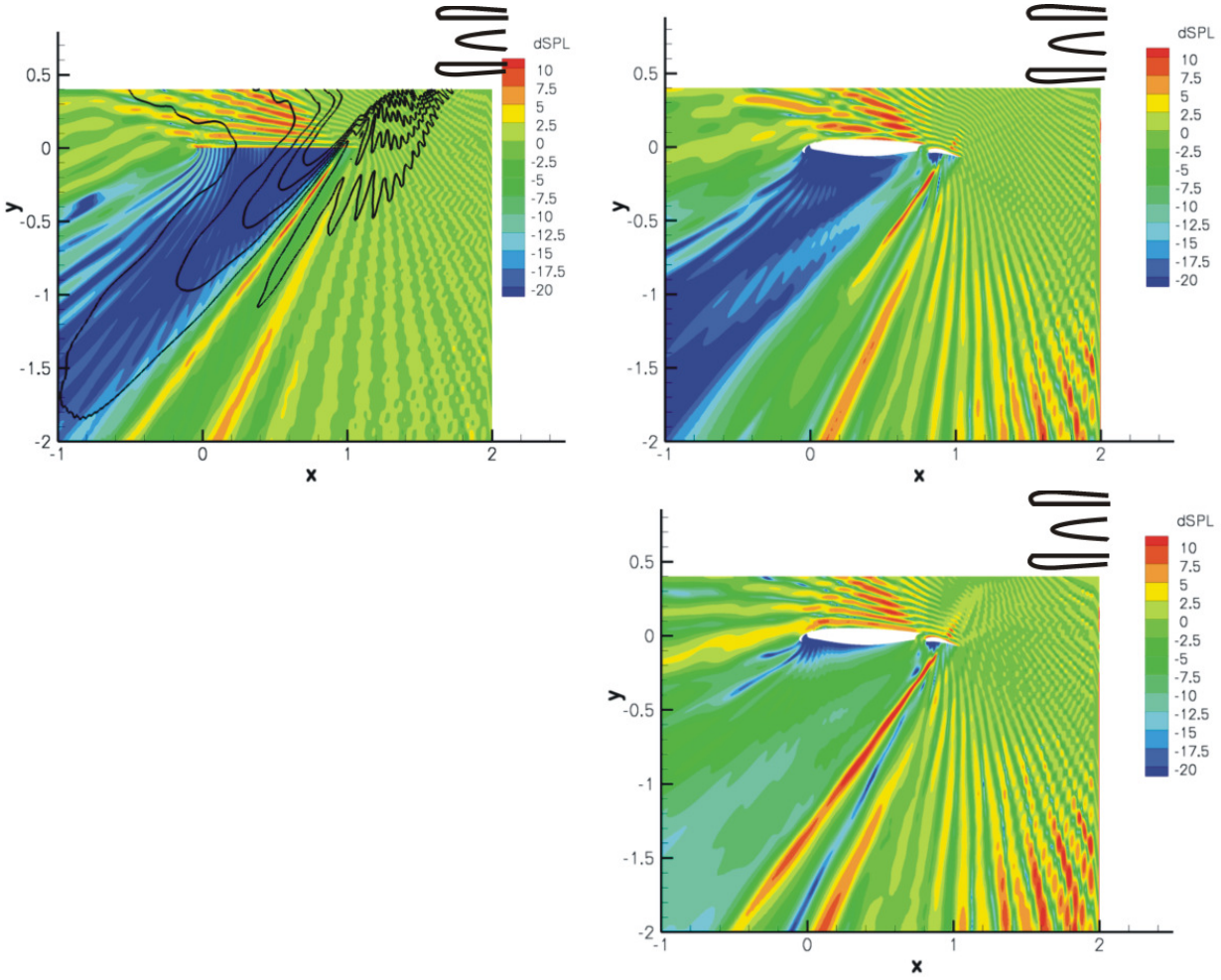

Figure 11. ***Pictures of ΔSPL for flat plate and const. mean flow (top left), 3-element high-lift wing and const. mean flow (top right), 3-element high-lift wing and viscous RANS mean flow (bottom right); for each figure the azimuthal fan mode 0 and the radial fan modes 1-4 are shown; in the left plot the iso-SPL lines for the free-field computation are plotted in black***

constant case. For the azimuthal modes $7-11$ there is no difference in ΔSPL between constant mean flow results and RANS mean flow results for shielding case "B" and "C".

Two main conclusions can be drawn:

- For constant mean flow one derive the same shielding benefit results for all obstacles which block the same area in the line of sight, i.e. the geometrical dimension is the most important parameter, not the detailed shape (flat plate vs. high-lift geometry).
- However, incorporating the effect of flow non-uniformities and gradients of the realistic viscous mean-flow significant differences are observed compared to simplified models based on uniform (i.e. constant) flow, i.e. the shielding potential is considerably overestimated by simplified propagation models, yielding up to $10dB$ difference.

V. Summary

A study about the influence of viscous mean flow on the shielding of rear-mounted engine-fan noise due to a 3-element high-lift wing has been conducted in this paper. For this a modified Thompson boundary condition was implemented into the CAA code PIANO. The modification was necessary to enable the coupling of the fan noise data into the CAA domain. It has been demonstrated that the modified Thompson

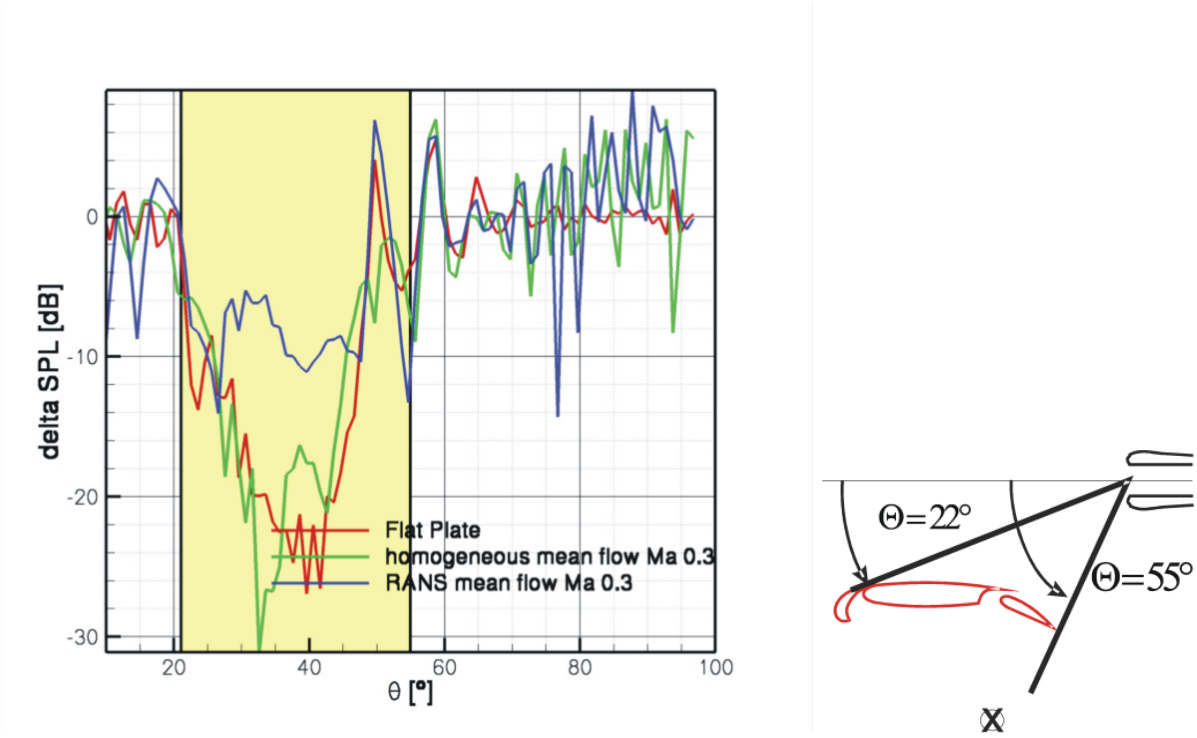

Figure 12. *ΔSPL due to shielding for the flat plate and wing for const. mean flow and for the wing with viscous RANS mean flow over the emission angle Θ on an observer circle with radius of 2 chord length; yellow highlighted area is the area where the wing is in line of sight (left); definition of the angle Θ and area where the wing lies in the line of sight (right).*

boundary condition meets the requirements as a coupling boundary well. The shielding computations were conducted using the finite differences CAA code PIANO solving the LEE. Three different set-ups were studied: computing shielding factor for a high-lift wing in viscous mean flow, a high-lift wing in constant mean flow and flat plate with the high lift wing's dimensions in constant mean flow. The analysis was done for 42 modal modes always summed up the modes with constant azimuthal mode. As conclusion it was shown, that the shape of the shielding obstacle has only minor influence on the shielding behavior. It could also be shown that there is a considerable influence due to shear layers and mean flow gradients on the shielding potential. The shielding potential is considerably overestimated approximating the mean flow through a uniform bulk velocity.

References

[1]C. Clancy and H.J. Rice. Acoustic shielding in low mach number potential flow incorporating a wake model using BEM. *AIAA Paper 2009-3174*, 2009.

[2]J. W. Delfs, M. Bauer, R. Ewert, H. A. Grogger, M. Lummer, and T. G. W. Lauke. Numerical Simulations of Aerodynamic Noise with DLR's aeroacoustic code PIANO. *PIANO*, handbook version 5.2, 2008.

[3]M. Howe. The influence of vortex shedding on the generation of sound by convected turbulence. *Journal of Fluid Mechanics, 711-740*, Vol. 76, No. 4, 1976.

[4]F. Q. Hu, M. Y. Hussaini, and J. L. Manthey. Low-dissipation and low-dispersion Runge-Kutta schemes for computational acoustics. *J. Comp. Phys.*, 124:177–191, 1996.

[5]D. Jones. Aerodynamic sound due to a source near a half-plane. *Journal of the Institute of Mathematics and Its Applications, 114-122*, Vol. 9, 1972.

[6]J. W. Kim and D. J. Lee. Generalized characteristic boundary conditions for computational aeroacoustics. *AIAA Journal*, 38(11):2040–2049, 2000.

[7]J. W. Kim and D. J. Lee. Characteristic interface conditions for multiblock high-order computation on singular structured grid. *AIAA Journal*, 41(12):2341–2348, 2003.

[8]J. W. Kim and D. J. Lee. Generalized characteristic boundary conditions for computational aeroacoustics, part 2. *AIAA Journal*, 42(1):47–55, 2004.

[9]S. LIDOINE and B. CARUELLE. Fan noise radiation from intake: Comparisons between fem predictions and fan rig test measurements with flare. *ICSV Lisbon 2005*, 2005.

[10]S. Redonnet, C. Mincu, and E. Manoha. Computational aeroacoustics of a realistic co-axial engine in subsonic and supersonic take-off conditions. *AIAA Paper 2009-3240*, 2009.

[11]J. Song and W. Chew. Large scale computations using fisc. *Antennas and Propagation Society International Symposium, 1856-1859*, Vol. 4, 2000.

[12]C. Tam and J. Webb. Dispersion-relation-preserving finite difference schemes for computational acoustics. *J. Comp. Phys.*, 107:262–281, 1993.

[13]Christopher. K. W. Tam. *Benchmark Problems and Solutions*. 1995. NASA CP 3300.

[14]Kevin W. Thompson. Time-dependent boundary conditions for hyperbolic systems. *J. Comp. Phys. 68, 1-24*, 1987.

[15]Kevin W. Thompson. Time-dependent boundary conditions for hyperbolic systems,ii. *J. Comp. Phys. 89, 439-461*, 1990.

Figures

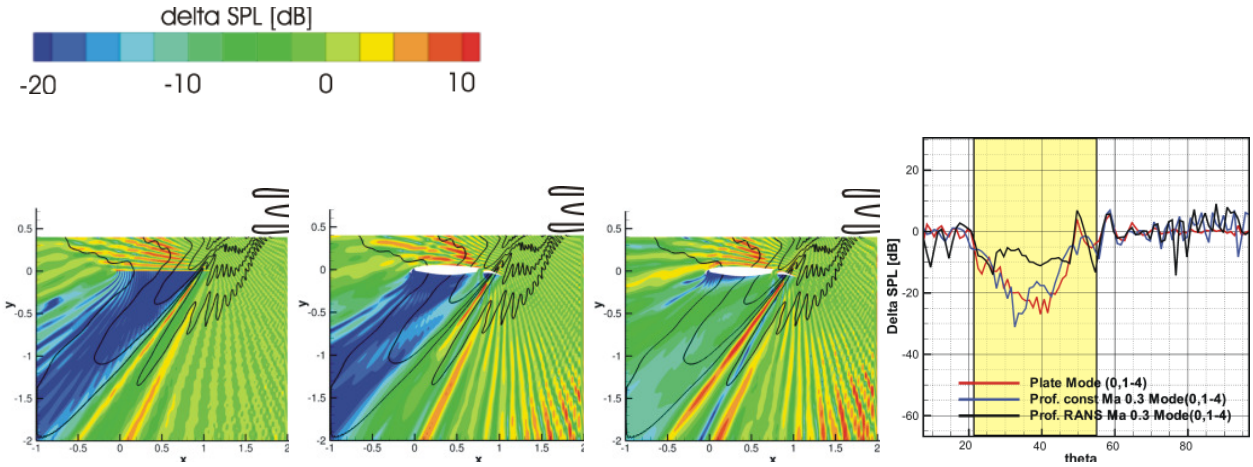

Figure 13. *Results for Modes(1-4,0); ΔSPL flat plate with const. mean flow (first); ΔSPL 3-element wing with const. mean flow (second);ΔSPL 3-element wing with viscous mean flow (third); ΔSPL over emission angle Θ (4th)*

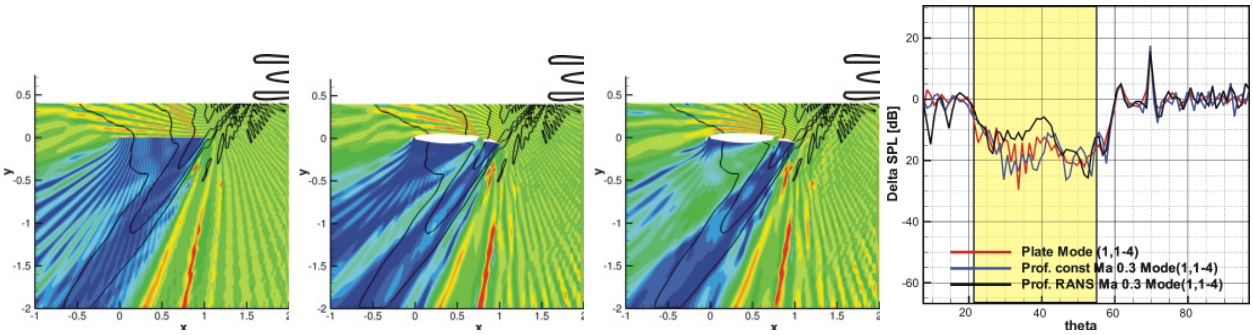

Figure 14. *Results for Modes(1-4,1); ΔSPL flat plate with const. mean flow (first); ΔSPL 3-element wing with const. mean flow (second);ΔSPL 3-element wing with viscous mean flow (third); ΔSPL over emission angle Θ (4th)*

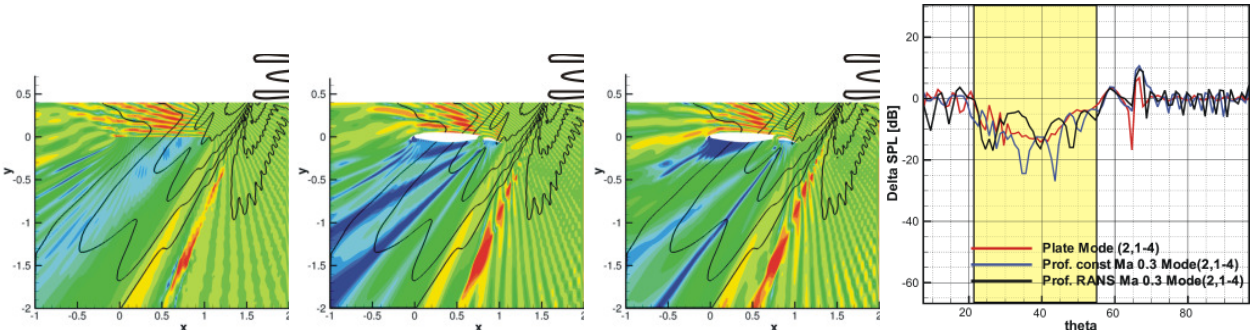

Figure 15. *Results for Modes(1-4,2); ΔSPL flat plate with const. mean flow (first); ΔSPL 3-element wing with const. mean flow (second);ΔSPL 3-element wing with viscous mean flow (third); ΔSPL over emission angle Θ (4th)*

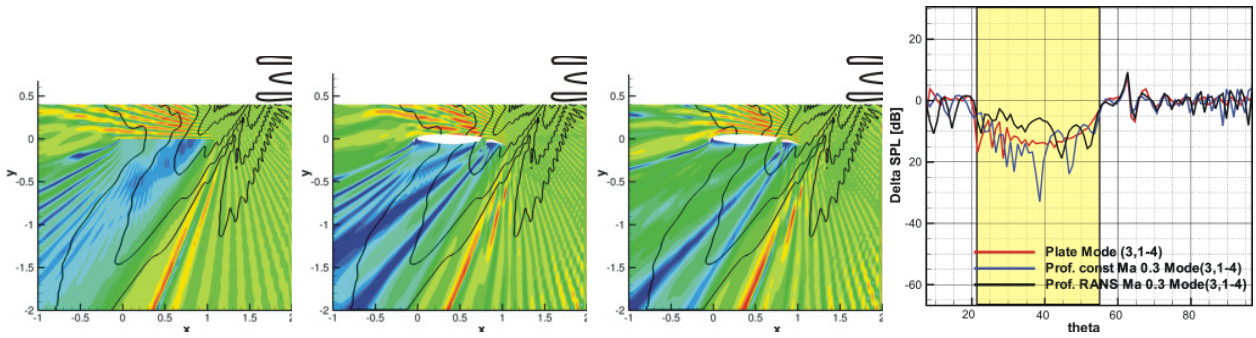

Figure 16. *Results for Modes(1-4,3); ΔSPL flat plate with const. mean flow (first); ΔSPL 3-element wing with const. mean flow (second);ΔSPL 3-element wing with viscous mean flow (third); ΔSPL over emission angle Θ (4th)*

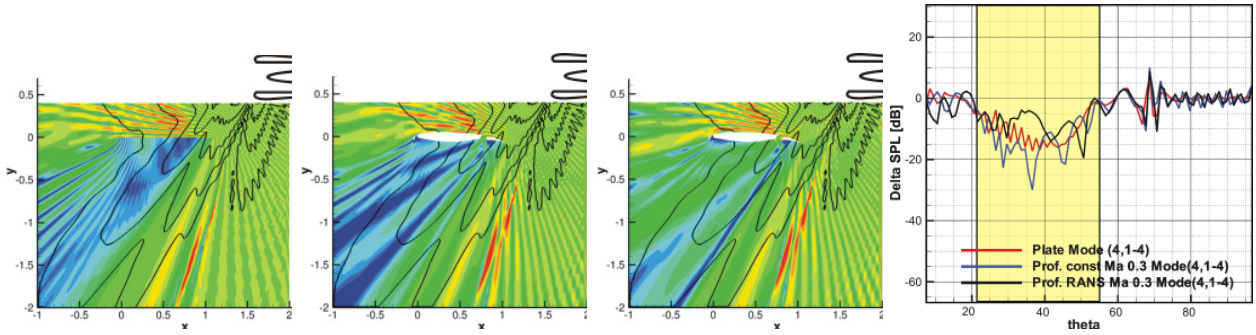

Figure 17. *Results for Modes(1-4,4); ΔSPL flat plate with const. mean flow (first); ΔSPL 3-element wing with const. mean flow (second);ΔSPL 3-element wing with viscous mean flow (third); ΔSPL over emission angle Θ (4th)*

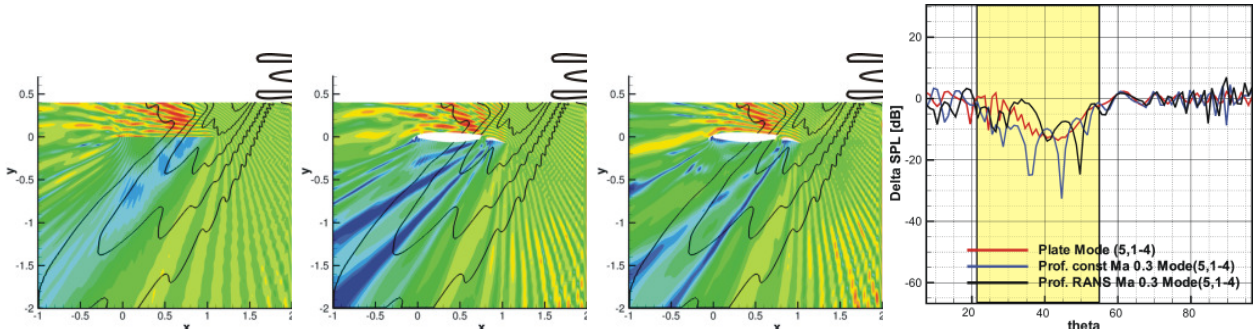

Figure 18. *Results for Modes(1-4,5); ΔSPL flat plate with const. mean flow (first); ΔSPL 3-element wing with const. mean flow (second);ΔSPL 3-element wing with viscous mean flow (third); ΔSPL over emission angle Θ (4th)*

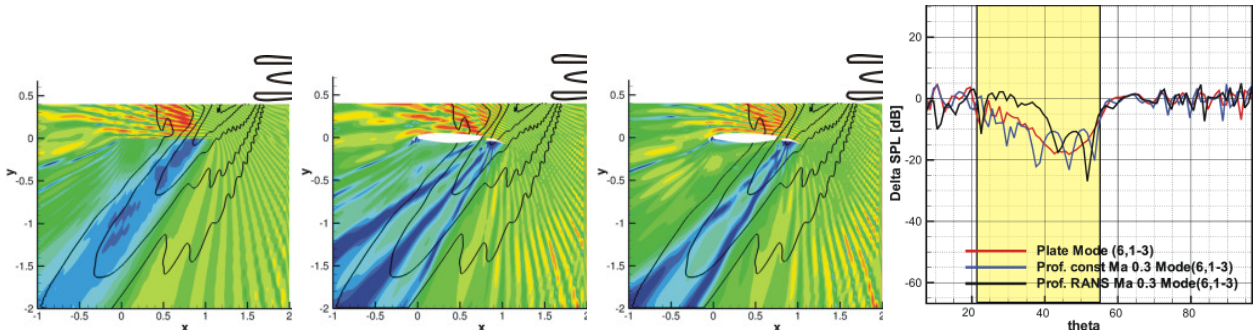

Figure 19. *Results for Modes(1-3,6); ΔSPL flat plate with const. mean flow (first); ΔSPL 3-element wing with const. mean flow (second);ΔSPL 3-element wing with viscous mean flow (third); ΔSPL over emission angle Θ (4th)*

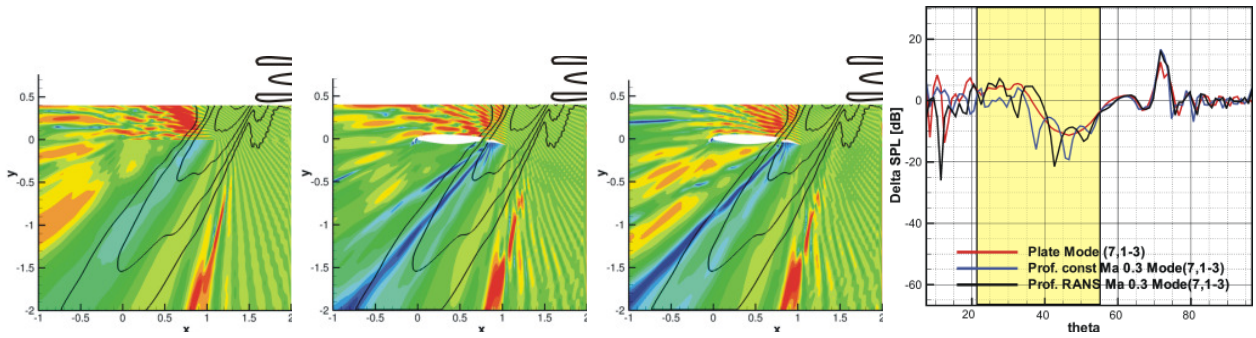

Figure 20. *Results for Modes(1-3,7); ΔSPL flat plate with const. mean flow (first); ΔSPL 3-element wing with const. mean flow (second);ΔSPL 3-element wing with viscous mean flow (third); ΔSPL over emission angle Θ (4th)*

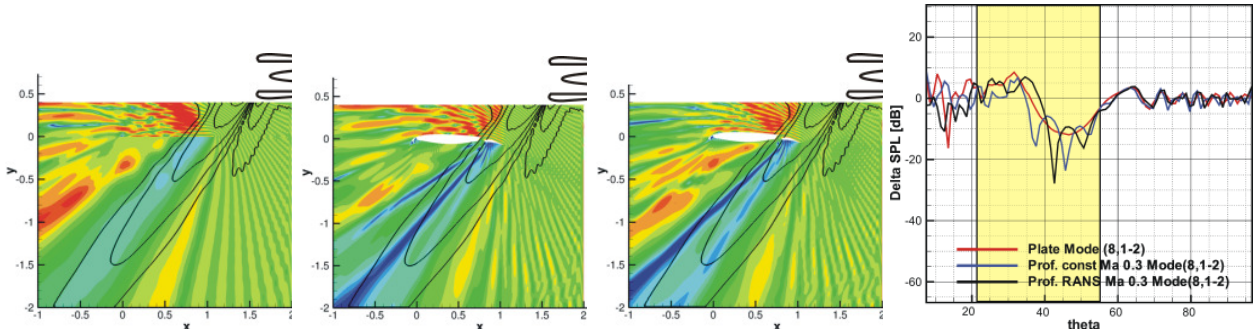

Figure 21. *Results for Modes(1-2,8); ΔSPL flat plate with const. mean flow (first); ΔSPL 3-element wing with const. mean flow (second);ΔSPL 3-element wing with viscous mean flow (third); ΔSPL over emission angle Θ (4th)*

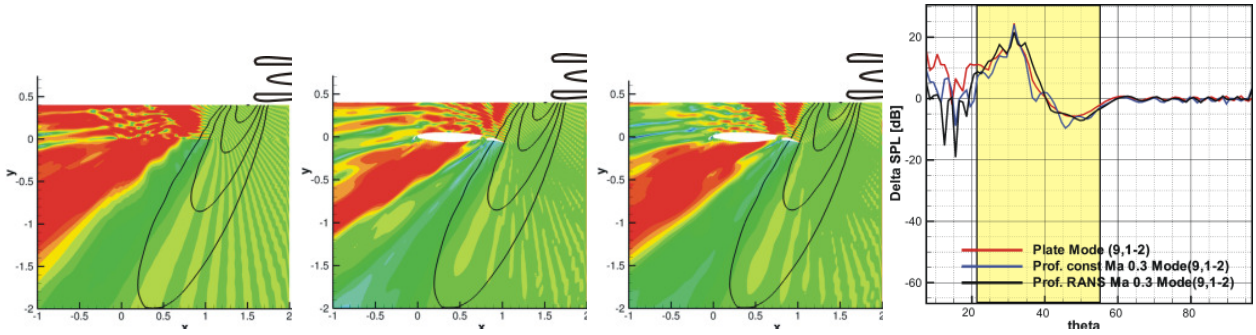

Figure 22. *Results for Modes(1-2,9); ΔSPL flat plate with const. mean flow (first); ΔSPL 3-element wing with const. mean flow (second);ΔSPL 3-element wing with viscous mean flow (third); ΔSPL over emission angle Θ (4th)*

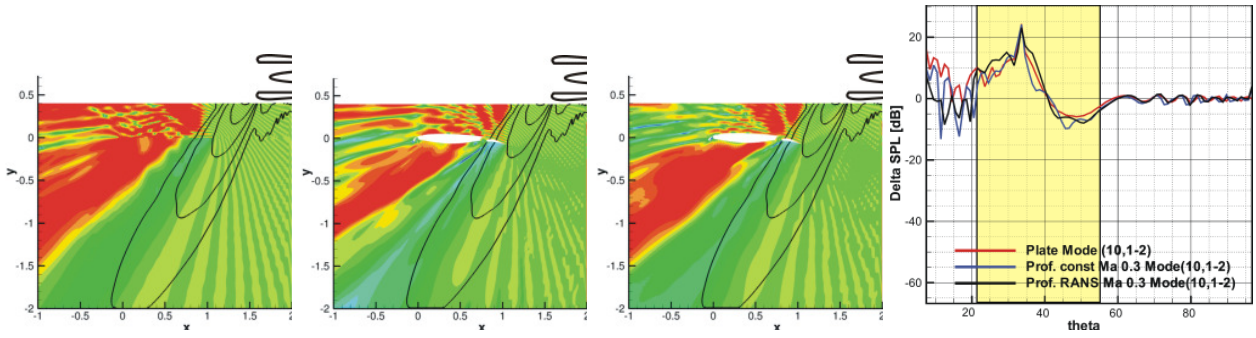

Figure 23. *Results for Modes(1-2,10); ΔSPL flat plate with const. mean flow (first); ΔSPL 3-element wing with const. mean flow (second);ΔSPL 3-element wing with viscous mean flow (third); ΔSPL over emission angle Θ (4th)*

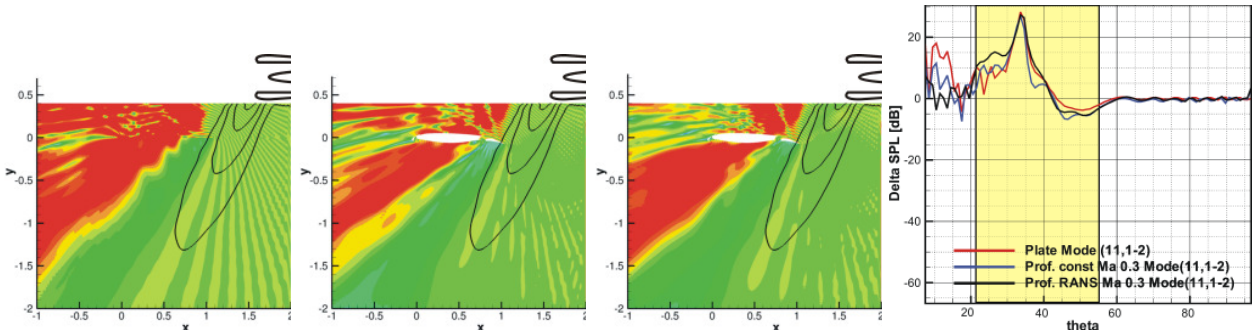

Figure 24. *Results for Modes(1-1,11); ΔSPL flat plate with const. mean flow (first); ΔSPL 3-element wing with const. mean flow (second);ΔSPL 3-element wing with viscous mean flow (third); ΔSPL over emission angle Θ (4th)*